



# Practical quantum imaging with undetected photons

EMMA PEARCE,<sup>1,\*</sup> NATHAN R. GEMMELL,<sup>1</sup> JEFFERSON FLÓREZ,<sup>1</sup> JIAYE DING,<sup>1</sup> RUPERT F. OULTON,<sup>1</sup> ALEX S. CLARK,<sup>1,2</sup> AND CHRIS C. PHILLIPS<sup>1</sup>

<sup>1</sup>Blackett Laboratory, Department of Physics, Imperial College London, SW7 2AZ, United Kingdom

<sup>2</sup>Quantum Engineering Technology Labs, H. H. Wills Physics Laboratory and Department of Electrical and Electronic Engineering, University of Bristol, BS8 1FD, United Kingdom

\* [e.pearce18@imperial.ac.uk](mailto:e.pearce18@imperial.ac.uk)

**Abstract:** Infrared (IR) imaging is invaluable across many scientific disciplines, from material analysis to diagnostic medicine. However, applications are often limited by detector cost, resolution and sensitivity, noise caused by the thermal IR background, and the cost, portability and tunability of infrared sources. Here, we describe a compact, portable, and low-cost system that is able to image objects at IR wavelengths without an IR source or IR detector. This imaging with undetected photons (IUP) approach uses quantum interference and correlations between entangled photon pairs to transfer image information from the IR to a wavelength which can be detected with a standard silicon camera. We also demonstrate a rapid analysis approach to acquire both phase and transmission image information. These developments provide an important step towards making IUP a commercially viable technique.

Published by Optica Publishing Group under the terms of the [Creative Commons Attribution 4.0 License](#). Further distribution of this work must maintain attribution to the author(s) and the published article's title, journal citation, and DOI.

## 1. Introduction

The infrared (IR) spectral region provides a wealth of information. In the near-IR and shortwave-IR (SWIR), higher harmonics of the vibrational modes of molecules and combinations of them can be probed. In the mid-IR, fundamental vibrational absorption bands occur, which provides greater molecular specificity [1,2] for quantitative chemical analysis. Sensing applications include studies of molecular structure [3], agriculture and food quality control [4,5], pharmaceutical monitoring [6], and biological imaging [7–9].

However, the IR is technologically poor in comparison with the visible, particularly at longer MIR wavelengths. IR cameras have much lower pixel counts than their silicon counterparts and, when operated at room temperature, are orders of magnitude noisier. Even expensive cryogenically-cooled IR detectors [10] are susceptible to noise arising from the ever-present 300 K black-body radiation background (the so-called BLIP limit).

One approach to avoiding IR cameras is to image the sample with IR photons which then undergo frequency up-conversion to wavelengths which can be detected with silicon before reaching the camera. However, this requires an IR source of photons and relies on high-power laser sources and/or cavities to combat the low conversion efficiencies [11,12]. This also leads to the sample being exposed to far more photons than are detected, which can be detrimental to photosensitive samples [13,14]. So-called ‘ghost imaging’ uses non-degenerate correlated photon pairs. The IR photon probes the sample before being detected with a single-channel IR detector whilst its partner at a silicon-detectable wavelength is logged by a camera [15,16]. Single-pixel IR detectors can also be used alongside computational imaging methods [17]. This circumvents some of the limitations of IR cameras, but it still suffers from the poor IR detector sensitivity, and from the influence of thermal IR background.

In contrast, the imaging with undetected photons (IUP) approach circumvents both the requirement to have a direct source of IR photons and the ability to detect them [18,19]. This works by generating photon pairs via spontaneous parametric down-conversion (SPDC) in a nonlinear crystal, where each pair consists of one silicon-detectable photon (signal) and one infrared photon (idler). By passing the pump through this crystal twice, it is possible to generate a pair in the first and/or second pass of the pump. If the signal photons from these two passes are precisely overlapped, and the idler photons are similarly overlapped, it is impossible to determine which pass generated the photon pair. This lack of ‘which-way’ (or indeed, ‘which-pass’) information means that optical interference is seen in the count rate of the signal photons. Blocking the idler beam from the first pass with an object effectively restores this ‘which-way’ information, destroying the interference. Note that coincident detection is not required, as merely the possibility to detect distinguishing information will impact the interference. The presence or absence of interference due to an object can therefore be readily recorded in the signal photon channel, i.e. using photons that have not themselves interacted with the object. Crucially, the image transfer process leaves the thermal background behind, allowing for detection sensitivities that are considerably improved over direct IR detection [20]. This principle has since been demonstrated for a variety of applications, including microscopy [21,22], hyperspectral imaging [23], spectroscopy [24–27], optical coherence tomography [28,29], and holography [30].

IUP certainly offers a promising alternative to direct infrared imaging, but it is important to address the potential barriers to practical implementation, and a literature is emerging that tackles issues of size, stability, and speed [30–32], with compact near- and mid-IR technologies already seeing use in environmental and agricultural studies [33,34].

Here, we demonstrate two generations of compact, fully self-contained, wavelength-tunable, and low cost devices for IUP, both of which enable SWIR imaging using only a basic silicon CMOS camera. We also discuss a rapid analysis approach which uses a pixel-wise Fourier transform to extract both transmission and phase information from as few as three image frames. These developments have allowed us to make dramatic reductions to the size, weight, cost, and power (SWaP-C) of IUP. By demonstrating the technology outside of a laboratory, we have also increased the technology readiness level of IUP.

## 2. Methods

Figure 1(a) shows the experimental setup of the first generation of our compact device. A 532 nm diode-pumped solid-state continuous-wave laser (CrystaLaser CL532-050) pumps a 10 mm-long periodically-poled lithium niobate (PPLN) crystal (Covesion MOPO515-0.5) with 35 mW of input power to produce signal and idler photons by type-0 SPDC. The pump is set to a beam diameter of  $\approx 0.45$  mm by lens L1 ( $f = 50$  mm) and is prepared in polarisation by a polarising beam splitter (PBS) and a half-wave plate (HWP). The dichroic mirror DM2 splits the idler photons from the signal and pump photons. The IR idler photons are sent to the sample, mounted on the sample mirror, while signal and pump photons propagate towards the scanning mirror, which is scanned to generate the interference fringes. All three wavelengths are then reflected back through the crystal, and as the pump makes its second pass, there is again a probability of generating a signal-idler photon pair.

As previously discussed, if the optical modes from the second pass are perfectly overlapped with those from the first then a sinusoidal modulation appears in the signal photon flux detected at the camera as the scanning mirror is moved. At these powers, the actual probability of generating a photon pair at each pass is low, allowing us to neglect the possibility of any stimulated down-conversion in the second process by photons originating from the first.

An object placed on the sample mirror can introduce a loss and/or phase change to the idler from the first pair, introducing distinguishability and a proportional change in the amplitude

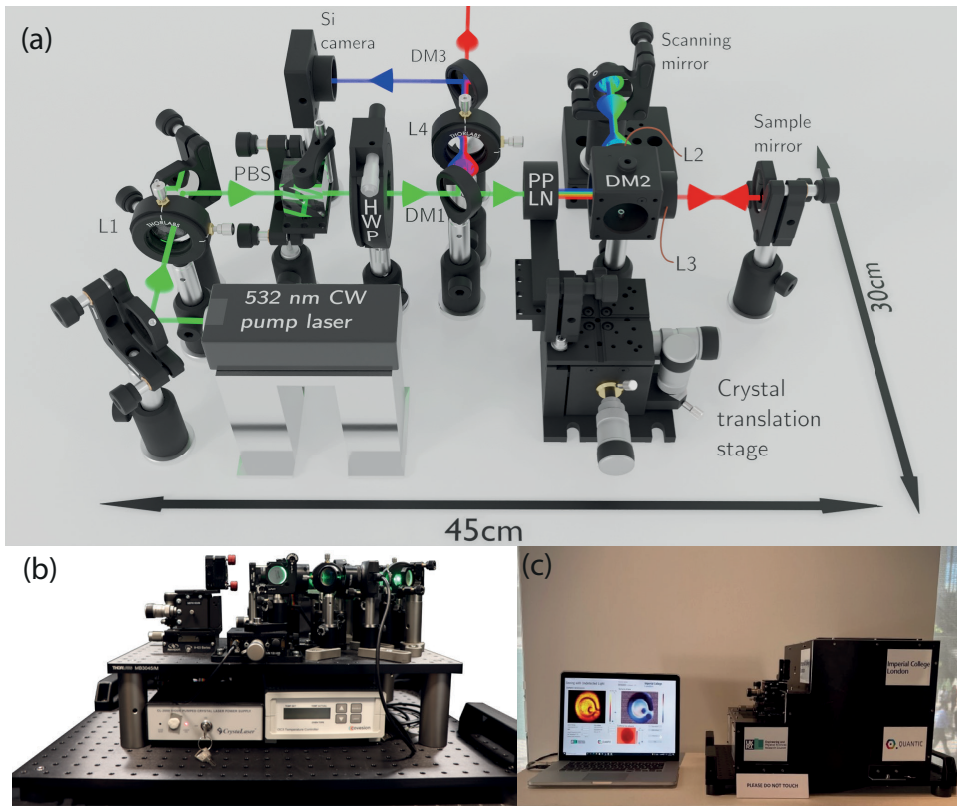


**Fig. 1.** (a) Schematic of a compact setup for imaging with undetected photons. Green indicates the pump beam. Blue and red represent signal (silicon-detectable) and idler (SWIR) beams, respectively. (b) Implementation of the compact device. The top breadboard ( $45 \times 30 \text{ cm}^2$ ) contains the imaging system, with an additional  $60 \times 45 \text{ cm}^2$  breadboard to house system controls. (c) Demonstration of imaging with undetected photons outside of a laboratory, featuring system enclosure and real-time analysis output to a graphical user interface.

and/or phase of the signal interference fringes. The amplitude variations can be imaged directly, but the phase changes are only detectable by moving the scanning mirror.

Both signal and idler photons are separated from the pump by dichroic mirror DM1 and sent to another dichroic mirror DM3, which sends only the signal photons to the camera. The idler photons go completely undetected. In fact, the silicon camera we use would not see them even if they were not removed by DM3.

To form the imaging system, each arm of the interferometer contains an  $f = 50 \text{ mm}$  focal length lens (L2 and L3) such that both sample and scanning mirrors are in the Fourier plane of the PPLN crystal, and the interferometer output is subsequently imaged onto the camera with a  $f = 75 \text{ mm}$  focal length lens. A number of camera frames are recorded at different scanning mirror positions, and the pixel-wise intensity variations are Fourier transformed [35], allowing the transmission and phase information of the object's IR response to be extracted.

The PPLN crystal can be translated perpendicular to the pump beam to access regions with different poling periods, each with transverse dimensions of  $0.5 \text{ mm} \times 0.5 \text{ mm}$ , in a way that tunes the signal and idler wavelengths. Also, it can be temperature tuned to further extend the

overall wavelength coverage, allowing us to generate signal photons from 706–839 nm and idler photons from 1455–2159 nm.

The whole system sits within a 60 cm × 45 cm footprint, and is 40 cm high (including all the laser and the temperature controlling and scanning electronics, Fig. 1(b)). An additional enclosure can be added to reduce background light and allow safe operation outside of a lab environment, as demonstrated in Fig. 1(c). In this case, the idler beam passes through an AR-coated silicon window (which is opaque to both pump and signal) to reach the sample which sits outside of the enclosure. While this window prevents pump leakage, it also allows us to make a useful analogy to applications which require imaging through silicon, such as in the device inspection industry [31,36]. Typically, no realignment was required after local transportation and, once aligned, the system can be operated by an untrained user assuming familiarity with the image acquisition software. The whole system is assembled from standard off-the-shelf components for ~£7000 (at time of purchase, 2021), excluding the laser. As the laser was purchased prior to the design of this system, its original price is not known but retails for approximately £2000 as of 2023.

### 3. Results

Figure 2 shows analysis of a thin-film gold interdigitated ring array microelectrode (Fig. 2(a), Micrux IDRA1) using 3 (d), 4 (e), 8 (f), and 15 (g) acquired images. In each case, the images are taken with a 200 ms exposure time at equally spaced piezo voltages over one oscillation of the interference pattern. The period of this oscillation is determined solely by the idler wavelength, as both signal and pump fields are scanned together, as shown in Fig. 2(b). The scanning mirror moves by close to half the idler wavelength, as the path is travelled twice. The detected wavelength is 808 nm, which is filtered using a 10 nm wide 810 nm bandpass filter, while the probe wavelength is 1559 nm. From fitting the edge spread function, we estimate a resolution of ~300 μm. The images have a pixel size of 5.2 × 5.2 μm<sup>2</sup> and are 1024 × 1280 pixels, i.e. somewhat greater than those available with current IR cameras.

From the analysed images in Fig. 2(d), it is clear that both the phase and amplitude features of the sample can be identified reliably, even when working right at the Nyquist limit when as few as 3 recorded images are used for the analysis. This approach drastically reduces both acquisition and processing times. We define visibility [37] as

$$\mathcal{V} = \frac{N_{max} - N_{min}}{N_{max} + N_{min}} = \frac{N_{amp}}{N_{mean}} = \frac{2F_1}{F_0}. \quad (1)$$

where  $N_{max}$  ( $N_{min}$ ) are the maximum (minimum) pixel values recorded on the camera during a phase scan,  $N_{mean}$  is the mean pixel value, and  $N_{amp}$  is the difference between  $N_{max}$  and  $N_{mean}$ . This can then be identified with outputs of a fast Fourier transform (FFT) to allow rapid calculation.  $F_1$  is the amplitude of the Fourier component corresponding to the frequency of the interference oscillation, and  $F_0$  is the amplitude of the DC Fourier component. The factor of 2 appears from including the negative frequency component calculated by the FFT. Contrast is defined as

$$C = N_{max} - N_{min} = 2N_{amp} = 4F_1. \quad (2)$$

Contrast is dependent on the overall brightness of a given system but can be a useful metric if there is a high detector noise floor as this will be subtracted, unlike the case with visibility. Phase is defined as

$$\phi = \arctan \frac{\text{Im}(F_1)}{\text{Re}(F_1)}. \quad (3)$$

Although as few as 3 images are sufficient for a qualitative analysis of the relative phase and transmission across a sample, unsurprisingly, more images improve accuracy if further parameter extraction is desired. No background subtraction is performed on the acquired images to remove

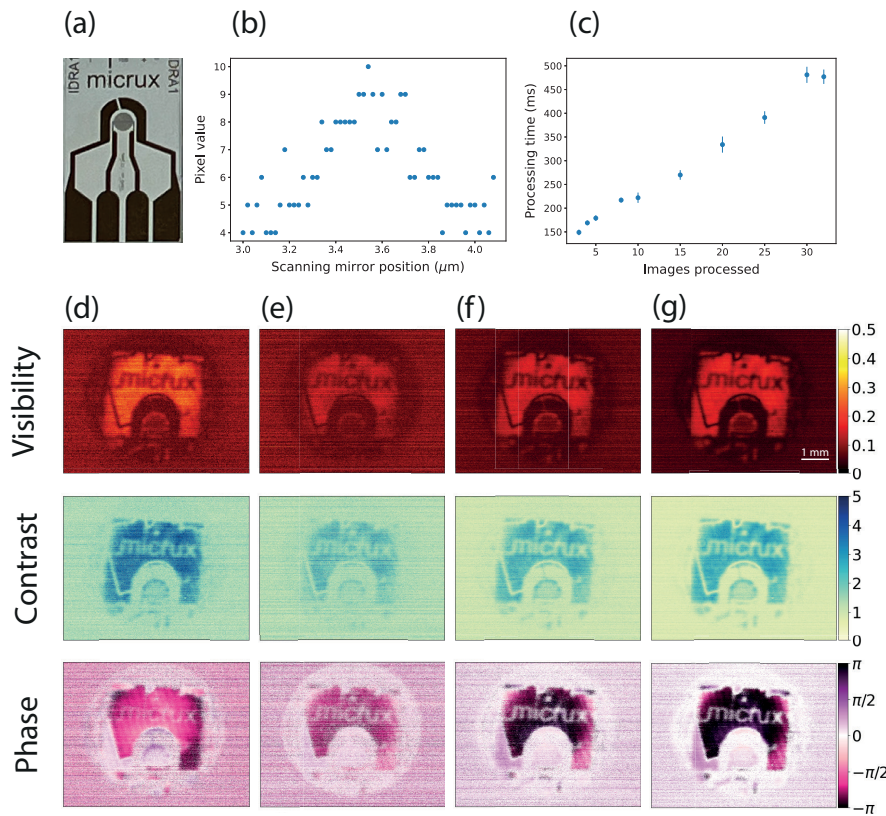


**Fig. 2.** (a) Visible image of an epoxy/gold interdigitated ring array microelectrode used as a test sample. (b) Typical interference fringe profile seen at one pixel of the camera as the scanning mirror is moved. (c) Time taken to calculate contrast, visibility, and phase from varying numbers of input images—times are averaged over 100 runs with error bars given by the standard deviation of these runs. Visibility, contrast, and phase profiles of the microelectrode shown in (a), generated from a pixel-wise Fourier transform of (d) 3, (e) 4, (f) 8, and (g) 15 images acquired while scanning the interferometer. Images were acquired with 200 ms exposure.

the noise floor, which leads to a lower visibility than seen in similar UPI demonstrations. Such a subtraction could be easily carried out with this system, albeit at the expense of longer processing times.

Phase imaging only provides numerically accurate results for slow changes in phase ( $\phi < 2\pi$  from pixel to pixel). While discontinuities in phase larger than this cannot be quantified exactly, the image still provides a qualitative picture of spatial phase changes. If the phase change results in a path delay that is larger than the coherence length, then the amplitude will also be affected allowing more information about the sample to be gained.

Features appear brighter in Fig. 2(d) compared to Fig. 2(e) due to where the frequency of the interference oscillation occurs on the Fourier transform sampling frequencies. Leakage into more than one Fourier component will be seen as a loss of signal and thus visibility will be reduced. This could be avoided by altering the Fourier transform length (via zero-padding) to better match the interference frequency to one of the sampled Fourier frequencies.

The time taken to perform the Fourier transform and calculate the above parameters is plotted against the number of input images in Fig. 2(c). The Fourier transform is implemented using a

Python wrapper of the fastest Fourier transform in the west (FFTW) [38,39] on a typical laboratory machine (Intel Xeon W-2102 processor, 4 cores). Processing times do not include saving or displaying the data. There is no delay between acquisitions required for image postprocessing [30] and we require both fewer images and shorter exposure times than seen in Ref. [31].

Another example of SWIR imaging using the same wavelengths and filtering is shown in Fig. 3, this time with an organic sample of a fly wing. This provides an object with continuously varying IR transmission across the image, rather than the example of the electrode which only has regions of either total transmission or no transmission. Both samples shown thus far have been measured in transmission. Regions of high visibility are seen where SWIR light passes through the sample to be reflected by the sample mirror. This requires that the path from the crystal to the sample mirror and the path from the crystal to the scanning mirror must be equal to within the SPDC coherence length ( $\approx 0.1$  mm). Any optical path length introduced by transmission through the sample must also be considered.

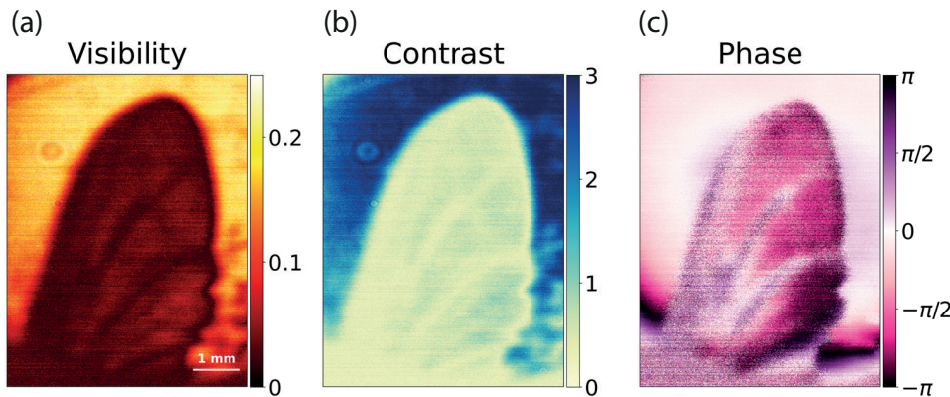


**Fig. 3.** (a) Visibility, (b) contrast, and (c) phase images of a fly wing, probed at 1559 nm and detected at 808 nm. Calculated from FFT of 55 acquired images.

Figure 4 shows the wavelength tunability of the system while imaging the gold contacts of the electrode, shown in the bottom half of Fig. 2(a). In Fig. 4(a), the crystal is kept at 125°C and the pump beam enters a region with a poling period of 7.40  $\mu\text{m}$ . These conditions result in a probe wavelength of 1558 nm and a detected wavelength of 808 nm (filtered with a 10 nm wide 810 nm bandpass). The crystal is then translated perpendicular to the pump beam to access a poling period of 7.71  $\mu\text{m}$  and heated to 200°C. This extends the probe wavelength to 1818 nm, beyond the sensitivity of a typical InGaAs camera, with the detection at 752 nm (filtered with a 10 nm wide 750 nm bandpass). The interferometer remains aligned throughout these types of wavelength sweep.

Both the spatial resolution ( $\Delta x = \frac{f_u \lambda_u}{\sqrt{2} \pi w_p}$ ) and magnification ( $M = \frac{f_c \lambda_d}{f_u \lambda_u}$ ) are reduced as the idler probe wavelength increases. Here,  $f_u$  is the focal length of the lens in the undetected path,  $f_c$  is the focal length of the lens in front of the camera,  $\lambda_d$  is the detected wavelength,  $\lambda_u$  is the undetected probe wavelength, and  $w_p$  is the beam waist of the pump [40]. The focal lengths of the lenses are also likely to vary from their nominal values as the wavelengths change. This change in magnification leads to all 4 contacts being visible in Fig. 4(b), while only 3 can be seen in Fig. 4(a), although chromatic aberrations in the lenses may also be limiting the resolution ( $\sim 450$   $\mu\text{m}$ ). Here the sample is being imaged in reflection, with high visibility in regions where the idler probe is reflected by the gold features, in which case it is the path from the crystal to the front face of the sample (rather than the sample mirror) that must be matched to the path from the crystal to the scanning mirror.

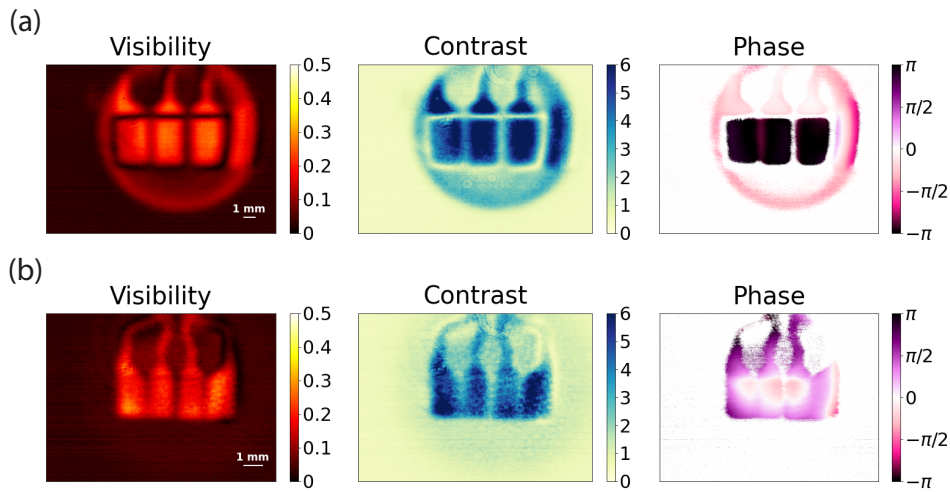


**Fig. 4.** Visibility, contrast, and phase of gold electrodes at different probe wavelengths, reached by translating crystal and adjusting temperature. (a) Probe wavelength 1558 nm and detected wavelength 808 nm. (b) Probe wavelength 1818 nm and detected wavelength 752 nm. All calculated from FFT of 55 acquired images.

#### 4. Further development: ‘EntangleCam’

Figure 5 shows the next design iteration of the system, the so-called ‘EntangleCam’, using smaller optomechanics and simplifying the layout by removing and combining some of the components. The PBS that was used in the previous system to filter the pump polarisation has been replaced by a laser line PBS with an AR coating that doubles as a dichroic mirror to separate the signal from pump. The lens in front of the camera has been removed so that the detector array samples the far-field of the crystal directly, and the original laser has been replaced by a simple 532 nm laser diode (OdicForce green laser module) providing less than 30 mW of light to the crystal. The pump shaping preparation is handled entirely by a single lens after the diode (beam diameter  $\approx 0.5$  mm), with a bandpass filter (BP) to eliminate any unwanted IR light.

The breadboard footprint has shrunk to  $30 \times 20 \text{ cm}^2$  and is only 15 cm high. The control electronics run from a single mains socket and add only  $25 \times 22.5 \times 7.5 \text{ cm}^3$  volume, while the total component cost is reduced to  $\sim \text{£6,000}$  (at time of purchase, 2022) including the laser. We note that both systems use basic CMOS cameras, rather than the sCMOS or EMCCD cameras typically used for imaging with undetected photons.

The system still retains the same wavelength tunability via crystal heating and translation with crystal translation stage (CTS), but even at a fixed room temperature, significant wavelength tunability is available. This is seen in Fig. 6, imaging another gold electrode sample (identical to that seen in Fig. 2), using only a room temperature crystal ( $24.5^\circ\text{C}$ ) without active temperature

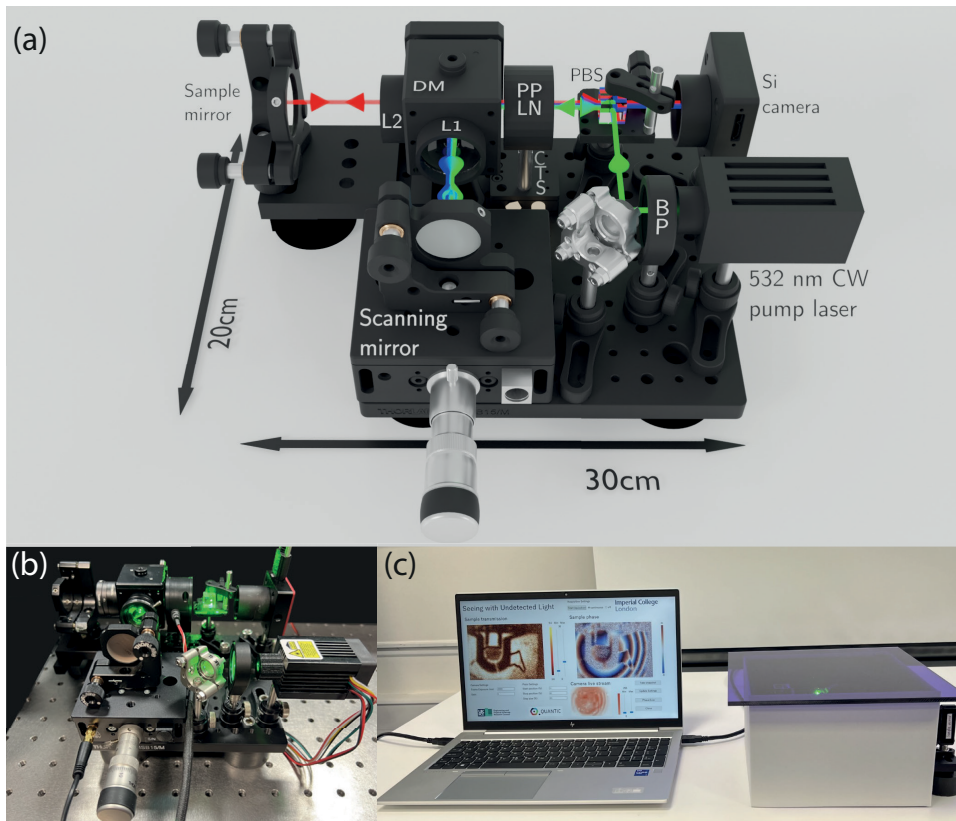


**Fig. 5.** (a) Schematic of second generation of compact imaging with undetected photons, with further reduced SWaP-C. Green indicates the pump beam. Blue and red represent signal (silicon-detectable) and idler (SWIR) beams, respectively. (b) Implementation of the second generation compact device. (c) Demonstration of the device outside of a laboratory, featuring system enclosure and real-time analysis output to a graphical user interface.

control. The bandpass filter on the camera was replaced with a long-pass filter to reject any residual pump light while also removing the need to change detection filters when moving between different poling periods. Without a bandpass filter, the visible bandwidth at the camera is approximately 20 nm. Images used in this analysis are taken with a 200 ms exposure time. Rings in the phase images are mainly attributed to spherical aberrations from lenses L1 and L2. The spatial resolution is found by fitting the edge spread function of the image features to give (a)  $\sim 200 \mu\text{m}$ , (b)  $\sim 400 \mu\text{m}$ , and (c)  $\sim 500 \mu\text{m}$ . No realignment is performed between wavelength changes and so this resolution could likely be improved by accounting for changes in focal length. It can be seen that despite the reduction in size, the system retains its imaging capabilities and broad tunability. This wavelength range is already relevant for biological imaging [22]. Depending on the probe wavelength desired for a particular application, this shows that the device could be designed to operate without any need for temperature control, further reducing SWaP-C.

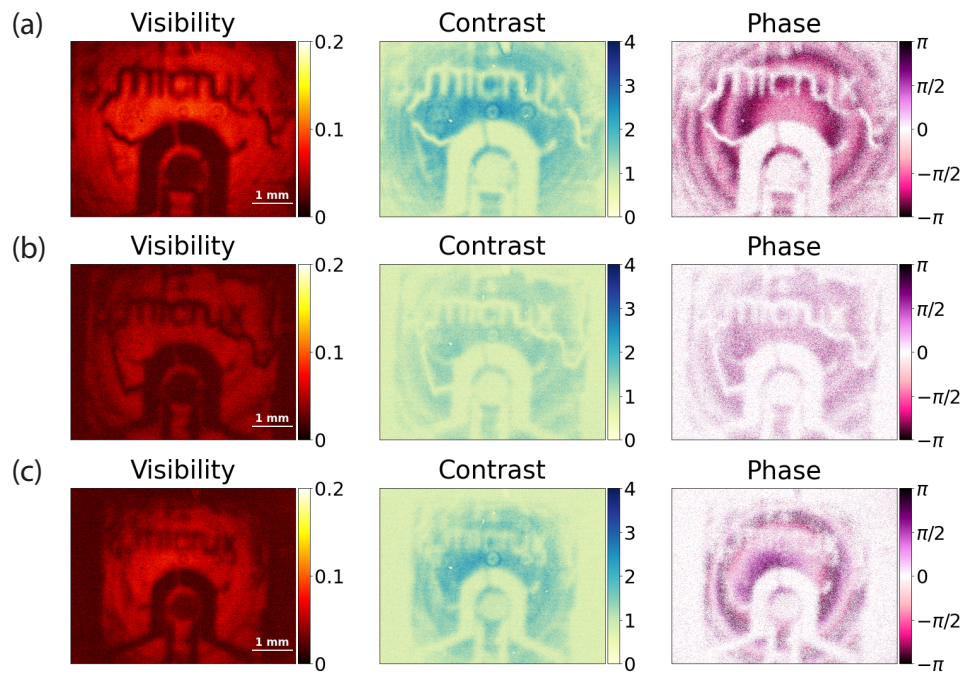


**Fig. 6.** Visibility, contrast, and phase of gold microelectrode at different probe wavelengths using the system in Fig. 5. Different wavelengths are reached by translating crystal whilst leaving its temperature at room temperature. (a) Probe wavelength 1450 nm and detected wavelength 840 nm. (b) Probe wavelength 1620 nm and detected wavelength 792 nm. (c) Probe wavelength 1783 nm and detected wavelength 758 nm. All calculated from FFT of 50 acquired images.

## 5. Discussion

In conclusion, we have demonstrated compact IUP systems that can perform infrared imaging with silicon-based detection and are robust and portable enough to be used outside of a laboratory environment. We have also demonstrated rapid analysis that allows a real-time quantitative measure of transmission and phase shift of a sample using as few as 3 recorded images. These systems represent a significant step forwards in the affordability and practicality of IUP as an alternative to direct IR imaging.

Future operation speeds could be enhanced by reducing the acquisition time required at each scanning mirror position, simply by using a higher power laser and/or a more sensitive camera. Both are readily available without major cost implications. Another route to increasing the number of photon pairs produced is by supplying a seed beam at the idler wavelength alongside the pump to stimulate the down-conversion in the crystal [41,42]. As well as the improvement in efficiency, the coherence length of the interferometer can be greatly extended if the seed beam itself has a long coherence length, such as a CW laser, which could allow measurements of thicker samples or at range [43].

While the time taken for the stage to move between positions, as well as a 100 ms pause for the stage to settle, is negligible in the overall speed of these systems, this may not be true if the above approaches lead to a drastic reduction in acquisition time. Alternatives to scanning include using polarisation optics to introduce different phases in one image [44] and off-axis holography techniques [45].

The spatial resolution of the system can be further enhanced by increasing the momentum correlations between the signal and idler photons; in the current configuration this would be achieved by increasing the width of the pump beam [40]. Additionally, positioning of the lenses can distort the coherence function [46] and it was not possible to match both focal lengths and path lengths with readily available commercial lenses. As the resolution of IUP improves [47], the high pixel count of the silicon cameras will become increasingly important. The spectral resolution of undetected photon techniques is typically defined by detection choices, such as bandpass filters used in the images above or a visible spectrometer for spectroscopic applications. The SPDC spectrum itself can be narrowed by using a longer crystal and/or narrower pump bandwidth [48].

Furthermore, there are a number of ways in which the operating wavelengths can be extended towards the mid-IR, including different pump wavelengths [14], different poling periods [49,50], and different nonlinear materials [27,51–53]. By moving towards the mid-IR, we anticipate our system will be a valuable tool for chemically and medically relevant applications [3,8,9,54].

**Funding.** Engineering and Physical Sciences Research Council (EP/T00097X/1, UF160475).

**Disclosures.** The authors declare no conflicts of interest.

**Data availability.** The data that support the findings of this study are available from the corresponding author upon reasonable request.

## References

1. K. B. Beć, J. Grabska, and C. W. Huck, “Near-infrared spectroscopy in bio-applications,” *Molecules* **25**(12), 2948 (2020).
2. Y. Ozaki, C. Huck, S. Tsuchikawa, *et al.*, *Near-Infrared Spectroscopy: Theory, Spectral Analysis, Instrumentation, and Applications* (Springer, 2021).
3. Q. Dong, C. Yu, L. Li, *et al.*, “Near-infrared spectroscopic study of molecular interaction in ethanol-water mixtures,” *Spectrochim. Acta, Part A* **222**, 117183 (2019).
4. F. García-Sánchez, L. Galvez-Sola, J. J. Martínez-Nicolás, *et al.*, “Using near-infrared spectroscopy in agricultural systems,” in *Developments in Near-Infrared Spectroscopy*, K. G. Kyriyanidis and J. Skvaril, eds. (IntechOpen, Rijeka, 2017), chap. 5.
5. V. Sileoni, O. Marconi, and G. Perretti, “Near-infrared spectroscopy in the brewing industry,” *Crit. Rev. Food Sci. Nutr.* **55**(12), 1771–1791 (2015).
6. M. Razuc, A. Graña, L. Gallo, *et al.*, “Near-infrared spectroscopic applications in pharmaceutical particle technology,” *Drug Dev. Ind. Pharm.* **45**(10), 1565–1589 (2019).
7. M. Ishigaki, T. Nishii, P. Puangchit, *et al.*, “Noninvasive, high-speed, near-infrared imaging of the biomolecular distribution and molecular mechanism of embryonic development in fertilized fish eggs,” *J. Biophotonics* **11**(4), e201700115 (2018).
8. R. Wang and Y. Wang, “Fourier transform infrared spectroscopy in oral cancer diagnosis,” *Int. J. Mol. Sci.* **22**(3), 1206 (2021).
9. G. Bellisola and C. Sorio, “Infrared spectroscopy and microscopy in cancer research and diagnosis,” *American Journal of Cancer Research* **2**, 1 (2012).
10. A. W. Rogalski, M. E. Kopytko, and P. M. Martyniuk, *Antimonide-Based Infrared Detectors: A New Perspective* (SPIE, 2018).
11. L. M. Kehlet, P. Tidemand-Lichtenberg, J. S. Dam, *et al.*, “Infrared upconversion hyperspectral imaging,” *Opt. Lett.* **40**(6), 938–941 (2015).
12. S. Junaid, S. C. Kumar, M. Mathez, *et al.*, “Video-rate, mid-infrared hyperspectral upconversion imaging,” *Optica* **6**(6), 702–708 (2019).
13. M. A. Taylor and W. P. Bowen, “Quantum metrology and its application in biology,” *Phys. Rep.* **615**, 1–59 (2016).
14. N. R. Gemmell, J. Flórez, E. Pearce, *et al.*, “Loss-compensated and enhanced midinfrared interaction-free sensing with undetected photons,” *Phys. Rev. Appl.* **19**(5), 054019 (2023).
15. R. S. Aspden, N. R. Gemmell, P. A. Morris, *et al.*, “Photon-sparse microscopy: visible light imaging using infrared illumination,” *Optica* **2**(12), 1049–1052 (2015).
16. C. C. Kim and G. Kanner, “Infrared two-color ghost imaging using entangled beams,” in *Quantum Communications and Quantum Imaging VII*, vol. 7815 R. E. Meyers, Y. Shih, and K. S. Deacon, eds., International Society for Optics and Photonics, p. 781503 (SPIE, 2010).
17. G. M. Gibson, B. Sun, M. P. Edgar, *et al.*, “Real-time imaging of methane gas leaks using a single-pixel camera,” *Opt. Express* **25**(4), 2998–3005 (2017).
18. X. Y. Zou, L. J. Wang, and L. Mandel, “Induced coherence and indistinguishability in optical interference,” *Phys. Rev. Lett.* **67**(3), 318–321 (1991).

19. G. B. Lemos, V. Borish, G. D. Cole, *et al.*, “Quantum imaging with undetected photons,” *Nature* **512**(7515), 409–412 (2014).
20. Y. Ma, N. Gemmell, E. Pearce, *et al.*, “Eliminating thermal infrared background noise by imaging with undetected photons,” *Phys. Rev. A* **108**(3), 032613 (2023).
21. I. Kviatkovsky, H. M. Chrzanowski, E. G. Avery, *et al.*, “Microscopy with undetected photons in the mid-infrared,” *Sci. Adv.* **6**(42), eabd0264 (2020).
22. A. Búzás, E. K. Wolff, M. G. Benedict, *et al.*, “Biological microscopy with undetected photons,” *IEEE Access* **8**, 107539–107548 (2020).
23. A. V. Paterova, S. M. Maniam, H. Yang, *et al.*, “Hyperspectral infrared microscopy with visible light,” *Sci. Adv.* **6**(44), eabd0460 (2020).
24. D. A. Kalashnikov, A. V. Paterova, S. P. Kulik, *et al.*, “Infrared spectroscopy with visible light,” *Nat. Photonics* **10**(2), 98–101 (2016).
25. C. Lindner, S. Wolf, J. Kiessling, *et al.*, “Fourier transform infrared spectroscopy with visible light,” *Opt. Express* **28**(4), 4426–4432 (2020).
26. P. Kaufmann, H. M. Chrzanowski, A. Vanselow, *et al.*, “Mid-IR spectroscopy with NIR grating spectrometers,” *Opt. Express* **30**(4), 5926–5936 (2022).
27. A. V. Paterova, Z. S. Toa, H. Yang, *et al.*, “Broadband quantum spectroscopy at the fingerprint mid-infrared region,” *ACS Photonics* **9**(6), 2151–2159 (2022).
28. A. V. Paterova, H. Yang, C. An, *et al.*, “Tunable optical coherence tomography in the infrared range using visible photons,” *Quantum Science and Technology* **3**(2), 025008 (2018).
29. A. Vanselow, P. Kaufmann, I. Zorin, *et al.*, “Frequency-domain optical coherence tomography with undetected mid-infrared photons,” *Optica* **7**(12), 1729–1736 (2020).
30. S. Töpfer, M. G. Bassett, J. Fuenzalida, *et al.*, “Quantum holography with undetected light,” *Sci. Adv.* **8**(2), eabl4301 (2022).
31. A. V. Paterova, H. Yang, Z. S. D. Toa, *et al.*, “Quantum imaging for the semiconductor industry,” *Appl. Phys. Lett.* **117**(5), 054004 (2020).
32. M. Gilaberte Basset, A. Hochrainer, S. Töpfer, *et al.*, “Video-rate imaging with undetected photons,” *Laser — Photonics Reviews* **15**(6), 2000327 (2021).
33. K. B. Beć, J. Grabska, H. W. Siesler, *et al.*, “Handheld near-infrared spectrometers: Where are we heading?” *NIR news* **31**(3-4), 28–35 (2020).
34. C. Hutengs, B. Ludwig, A. Jung, *et al.*, “Comparison of portable and bench-top spectrometers for mid-infrared diffuse reflectance measurements of soils,” *Sensors* **18**(4), 993 (2018).
35. M. Kutas, B. Haase, J. Klier, *et al.*, “Quantum-inspired terahertz spectroscopy with visible photons,” *Optica* **8**(4), 438–441 (2021).
36. M. Hazel and M. Karpman, “Measuring mems through silicon caps,” *Reliability, Packaging, Testing, and Characterization of MEMS/MOEMS VII* **6884**, 68840F (2008).
37. J. D. Ellis, “Field guide to displacement measuring interferometry,” (2014).
38. M. Frigo and S. G. Johnson, “The design and implementation of FFTW3,” *Proc. IEEE* **93**(2), 216–231 (2005).
39. H. Gomersall, pyFFTW documentation, <https://doi.org/10.5281/zenodo.59508> (2016). Accessed 20 June 2023.
40. J. Fuenzalida, A. Hochrainer, G. B. Lemos, *et al.*, “Resolution of quantum imaging with undetected photons,” *Quantum* **6**, 646646 (2022).
41. Y. Michael, I. Jonas, L. Bello, *et al.*, “Augmenting the sensing performance of entangled photon pairs through asymmetry,” *Phys. Rev. Lett.* **127**(17), 173603 (2021).
42. J. Flórez, E. Pearce, N. R. Gemmell, *et al.*, “Enhanced nonlinear interferometry via seeding,” *arXiv*, arXiv:2209.06749 (2022).
43. A. C. Cardoso, L. Beruezo, D. Ávila, *et al.*, “Classical imaging with undetected light,” *Phys. Rev. A* **97**(3), 033827 (2018).
44. B. E. Haase, J. Hennig, M. Kutas, *et al.*, “Phase-quadrature quantum imaging with undetected photons,” *Opt. Express* **31**(1), 143–152 (2023).
45. O. Wolley, S. Mekhail, P.-A. Moreau, *et al.*, “Near single-photon imaging in the shortwave infrared using homodyne detection,” *Proc. Natl. Acad. Sci. U. S. A.* **120**(10), e2216678120 (2023).
46. A. Hochrainer, M. Lahiri, R. Lapkiewicz, *et al.*, “Interference fringes controlled by noninterfering photons,” *Optica* **4**(3), 341–344 (2017).
47. I. Kviatkovsky, H. M. Chrzanowski, and S. Ramelow, “Mid-infrared microscopy via position correlations of undetected photons,” *Opt. Express* **30**(4), 5916–5925 (2022).
48. A. Paterova, S. Lung, D. A. Kalashnikov, *et al.*, “Nonlinear infrared spectroscopy free from spectral selection,” *Sci. Rep.* **7**(1), 42608 (2017).
49. Z. S. D. Toa, A. V. Paterova, and L. A. Krivitsky, “Broadband diffraction of correlated photons from crystal superlattices,” *Quantum Sci. Technol.* **7**(1), 01LT01 (2022).
50. E. Ramos-Irsrade, K. Garay-Palmett, and R. S. Cudney, “Randomly aperiodically poled LiNbO<sub>3</sub> crystal design by Monte Carlo–Metropolis with simulated annealing optimization for ultrabroadband photon pair generation,” *Appl. Opt.* **60**(34), 10587–10593 (2021).

51. M. Kumar, P. Kumar, A. Vega, *et al.*, "Mid-infrared photon pair generation in AgGaS<sub>2</sub>," *Appl. Phys. Lett.* **119**(24), 244001 (2021).
52. Y. Mukai, R. Okamoto, and S. Takeuchi, "Quantum fourier-transform infrared spectroscopy in the fingerprint region," *Opt. Express* **30**(13), 22624–22636 (2022).
53. S. Lopez-Huidobro, M. Lippl, N. Y. Joly, *et al.*, "Fiber-based biphoton source with ultrabroad frequency tunability," *Opt. Lett.* **46**(16), 4033–4036 (2021).
54. H. Amrania, L. Woodley-Barker, K. Goddard, *et al.*, "Mid-infrared imaging in breast cancer tissue: an objective measure of grading breast cancer biopsies," *Converg. Sci. Phys. Oncol.* **4**(2), 025001 (2018).